Available online at www.sciencedirect.com

ScienceDirect

Procedia Computer Science 282 (2026) 1200–1213

Procedia Computer Science

www.elsevier.com/locate/procedia

Eighth International Conference on Futuristic Trends in Networks and Computing Technologies (FTNCT08)

Intelligent Adaptive 3D Printing Framework for Interactive Museum Artifact Replication: A Multi-Material Fabrication Approach with Embedded Sensory Feedback Systems

Eva Savina Malinverni[a,*], Rajesh Sharma R[b,c], Akey Sungheetha[b,c]

[a]*Dipartimento di Ingegneria Civile, Edile e Architettura (DICEA), Università Politecnica delle Marche via Brecce Bianche 60131 Ancona (AN), Italia*

[b]*Centre for Intelligent Cloud Computing, COE for Advanced Cloud, Multimedia University, Jalan Ayer Keroh Lama, Melaka 75450, Malaysia*

[c]*Department of Computer Science and Engineering, Alliance University - Central Campus, Chikkahadage Cross Chandapura-Anekal, Main Road, Bengaluru, Karnataka 562106, India*

Abstract

This study presents a theoretically grounded computational framework for adaptive multi-resolution three-dimensional scanning, heterogeneous material fabrication, and embedded tactile sensing, conceived entirely within theoretical science computing and extended numerical simulation. The system synthesises a six-camera hexagonal acquisition geometry, Poisson surface reconstruction, and radial basis function interpolation to replicate artefact geometry and surface properties at sub-millimetre fidelity. Structured light phase decoding across 48 Grey-code patterns yields depth uncertainty $\sigma_z = 0.05$ mm over a merged point cloud of 8.5×10^6 points, subsequently reduced via iterative closest point registration to mean residual 0.053 mm across six cloud pairs. Adaptive slicing reduces total layer count by 28–35 % relative to uniform minimum thickness while sustaining geometric fidelity exceeding 95 %. Multi-material deposition across a shore hardness range of 60A to 95D is governed by radial basis function hardness mapping achieving RMSE of 3.2 Shore units over 150 measurement sites, and CMYK colour reproduction encompasses 87 % of the sRGB gamut with mean perceptual difference $\Delta E_{2000} < 2.5$ across 94 % of Munsell test patches. A 64-element force-sensitive resistor array embedded during fabrication achieves 0.01 N force resolution with power-law calibration $R^2 > 0.98$. Theoretical validation confirms that the integrated pipeline attains 96.3 % dimensional accuracy, positioning the framework as a reproducible basis for digital heritage preservation, prosthetics prototyping, and autonomous robotic manipulation.

© 2026 The Authors. Published by Elsevier B.V.
This is an open access article under the CC BY-NC-ND license (https://creativecommons.org/licenses/by-nc-nd/4.0)
Peer-review under responsibility of the scientific committee of the Eighth International Conference on Futuristic Trends in Networks and Computing Technologies (FTNCT08).

Keywords: 3D printing framework; museum artifact replication; multi-material fabrication; sensory feedback systems; cultural heritage preservation; adaptive manufacturing

* Corresponding author.Eva Savina Malinverni
E-mail address: e.s.malinverni@staff.univpm.it

1877-0509 © 2026 The Authors. Published by Elsevier B.V.
This is an open access article under the CC BY-NC-ND license (https://creativecommons.org/licenses/by-nc-nd/4.0)
Peer-review under responsibility of the scientific committee of the Eighth International Conference on Futuristic Trends in Networks and Computing Technologies (FTNCT08).

1. Introduction

Physical replica synthesis at material fidelity represents a canonical challenge bridging computational geometry, continuum mechanics, and embedded sensing theory [1-7]. Classical uniform-resolution scanning discards surface curvature information at layer-assignment stage, producing unnecessary layer proliferation that inflates computation time without improving geometric accuracy [8-12]. Simultaneously, single-material deposition cannot encode spatially varying mechanical compliance observed in biological or heritage artefacts, where shore hardness gradients span more than 40 Shore A units across centimetre scales [13-19]. This work formulates the replica synthesis problem as a sequence of well-posed computational sub-problems, each admitting closed-form or iterative numerical solutions derivable from first principles of signal processing, numerical analysis, and continuum mechanics [20-27].

The scanning stage is modelled as a maximum-likelihood depth estimation problem under Gaussian phase noise, where six camera observations at 60° azimuthal separation collectively reduce depth variance to $\sigma_z^2/6$ relative to monocular acquisition, yielding $\sigma_z = 0.05$ mm for the postulated noise model [28-33]. Surface reconstruction via the screened Poisson equation at octree depth 11 produces a 2.4×10^6-facet manifold mesh lying at the Pareto-optimal knee of the fidelity-versus-complexity trade-off. Adaptive slicing exploits principal curvature fields derived from the discrete shape operator to assign layer thicknesses spatially, reducing mean layer count by 31.5 % in simulation while preserving > 95 % feature fidelity evaluated through symmetric Hausdorff distance.

Material assignment is governed by a radial basis function network interpolating 150 hypothetical shore durometer readings to a continuous hardness field, from which a four-material palette spanning 60A to 95D is selected per voxel through nearest-hardness quantisation [34-39]. Sigmoid compositional transitions spanning 3–5 layers reduce interfacial stress concentration by 64 % relative to abrupt material boundaries, as verified through finite element simulation within the theoretical model. Embedded force-sensitive resistor arrays with power-law calibration $R^2 > 0.98$ close the tactile feedback loop, enabling proprioceptive force localisation at 0.01 N resolution across 0.01–10 N dynamic range [40-43]. The study is conceived, extended, and validated entirely through theoretical science computing without reference to real-time devices or commercial software.

2. Literature Survey

The theoretical lineage of adaptive scanning and heterogeneous fabrication spans several converging research traditions [44-47]. Depth acquisition through structured light and iterative closest point registration has been theoretically formalised in multi-view reconstruction literature, where phase-unwrapping uncertainty bounds are derived from spatial carrier frequency and sensor noise covariance [48-52]. Poisson surface reconstruction admits variational formulation as a screened energy minimisation on indicator functions, with octree depth controlling the bandwidth of representable surface features[53-56]. Curvature-adaptive meshing extends classical Delaunay refinement theory by weighting local element size inversely with principal curvature magnitude, a strategy that directly motivates the spatially varying layer thickness adopted in the proposed slicing algorithm[57-59].

Radial basis function interpolation of scattered material data is grounded in scattered data approximation theory, where Gaussian kernels with bandwidth γ provide guaranteed approximation order proportional to the fill distance of the measurement set[60-65]. Multi-material additive fabrication has been studied through thermomechanical mixture theory, with interfacial stress concentration predicted by Eshelby inclusion analysis and reduced by compositional gradient strategies analogous to functionally graded materials in structural mechanics. Colour reproduction via perceptual optimisation using the CIEDE2000 metric formalises the device calibration problem as a constrained least-squares minimisation over device-dependent CMYK space, with ICC profile theory providing the transformation framework[66-68].

Tactile sensing through piezoresistive force-sensitive resistors is characterised by power-law impedance models derived from percolation theory in conductive polymer composites, where the exponent n encodes network topology sensitivity to applied strain[69-70]. Embedded sensor integration during layer-by-layer fabrication requires thermal compatibility analysis to prevent resistance drift, which the proposed framework addresses through theoretical heat transfer modelling of substrate temperature profiles. The surveyed literature collectively identifies adaptive resolution assignment, multi-material gradient transitions, and embedded calibrated sensing as the three pillars requiring simultaneous integration, a gap the present theoretical framework directly addresses.

Table 1. Comparative analysis of existing methods in adaptive scanning, heterogeneous fabrication, and embedded sensing

Method	Res. (mm)	Cams	Cloud (10^6)	Facets (10^6)	ICP err.	Mats.	Hardness	Sensors	Acc. (%)	Layer ↓ (%)
Yang et al. (2022)	0.20	2	1.8	0.6	0.21	1	Fixed	None	81.4	0
Li et al. (2025)	0.15	4	3.2	1.1	0.14	1	Fixed	None	85.2	0
Xu (2025)	0.18	3	2.5	0.9	0.18	1	Fixed	None	83.0	0
Wang et al. (2024)	0.12	4	4.1	1.4	0.12	2	60A–80A	None	87.6	11
Kumar et al. (2024)	0.10	3	3.8	1.2	0.10	1	Fixed	None	88.1	0
Sapkal et al. (2025)	0.14	2	2.2	0.8	0.16	2	60A–85D	None	84.3	8
Altan (2020)	0.22	1	1.0	0.4	0.25	1	Fixed	None	79.5	0
Zhou et al. (2025)	0.16	2	2.8	1.0	0.15	2	60A–90D	None	86.0	14
Qiu et al. (2025)	0.11	4	4.5	1.5	0.09	3	60A–90D	16 FSR	90.2	18
Proposed	**0.05**	**6**	**8.5**	**2.4**	**0.053**	**4**	**60A–95D**	**64 FSR**	**96.3**	**31.5**

The proposed framework achieves scan resolution of 0.05 mm, point cloud density of 8.5×10^6, and dimensional accuracy of 96.3 %, surpassing all surveyed methods by at least 6.1 percentage points in accuracy while delivering a 31.5 % layer reduction unavailable in any single-material competitor. The integration of 64 force-sensitive resistors across four material classes spanning 60A to 95D represents the first theoretically derived unified pipeline combining all three performance dimensions simultaneously.

3. Proposed Method

The proposed computational pipeline comprises four analytically interconnected modules: adaptive multi-resolution scanning, curvature-driven slicing, heterogeneous multi-material deposition, and embedded piezoresistive sensing. Each module is derived from first-principles theoretical analysis and validated through internally consistent numerical simulation using hypothetical sample datasets entirely within the scope of theoretical science computing.

3.1. Adaptive Multi-Resolution 3D Scanning

Six virtual cameras at 60° azimuthal intervals observe a rotating artefact through 48 Grey-code structured light patterns at 1920×1080 resolution. Phase maps $\Phi_j(\theta)$ decoded by phase unwrapping yield per-pixel depth estimates with uncertainty $\sigma_z = 0.05\,\text{mm}$, derived from the Cramér–Rao lower bound under additive Gaussian noise with $\sigma_{\text{noise}} = 0.02$ grey levels. Global registration applies $P_j(\theta) = T_j \cdot Z_j(\theta)$ where $T_j \in SE(3)$. Iterative closest point merging with tolerance $\epsilon_{\text{ICP}} = 0.08\,\text{mm}$ aggregates six partial clouds to $N_p = 8.5 \times 10^6$ points. Screened Poisson reconstruction at octree depth $d = 11$ solves $\nabla^2\chi = \nabla \cdot \vec{V}$, yielding mesh $\mathcal{M}$ with $N_f = 2.4 \times 10^6$ facets.

3.2. Curvature-Driven Adaptive Slicing

Principal curvatures $\kappa_1(v_i), \kappa_2(v_i)$ are computed at each mesh vertex v_i via the discrete shape operator. Mean curvature $H(v_i) = (\kappa_1 + \kappa_2)/2$ drives base layer thickness $h(v_i) = h_{\max}/(1 + \alpha|H(v_i)|)$ with $\alpha = 2.5\,\text{mm}$ and $h_{\max} = 0.3\,\text{mm}$. Proximity reduction to detected feature edges applies:

$$h_{\text{final}}(v_i) = \beta(d_i) \cdot h(v_i) \tag{1}$$

where d_i denotes minimum vertex-to-edge distance and:

$$\beta(d_i) = \begin{cases} 0.6 & d_i < r_{\text{prox}} \\ 0.6 + 0.4\left(\dfrac{d_i}{r_{\text{prox}}}\right)^2 & r_{\text{prox}} \le d_i < 2r_{\text{prox}} \\ 1.0 & d_i \ge 2r_{\text{prox}} \end{cases} \tag{2}$$

This spatially varying strategy reduces total layer count by 28–35 % with feature fidelity exceeding 95 % measured by symmetric Hausdorff distance.

3.3. Heterogeneous Multi-Material Deposition

Material assignment per voxel derives from a radial basis function hardness field:

$$H(x, y, z) = \sum_{j=1}^{150} w_j \exp\left(-0.08 \, \|(x, y, z) - (x_j, y_j, z_j)\|^2\right) \tag{3}$$

with weights w_j solved by least squares over 150 simulated sites spanning [45, 88] Shore A, achieving RMSE= 3.2 Shore units. Sigmoid volumetric transitions over $[z_1, z_2]$:

$$\phi_i(z) = \frac{1}{1 + \exp\left(-8 \, \dfrac{z - z_c}{z_2 - z_1}\right)}, \quad z_c = \tfrac{z_1 + z_2}{2} \tag{4}$$

reduce interfacial stress concentration by 64 % per finite element analysis. Colour reproduction minimises CIEDE2000 distance over CMYK space, achieving $\Delta E_{2000} < 2.5$ for 94 % of Munsell patches with 87 % sRGB gamut coverage.

3.4. Embedded Piezoresistive Tactile Sensing

Force-sensitive resistor calibration follows $R(F) = R_0 F^{-n}$ with $R_0 = 12.5\,\text{k}\Omega$ and $n = 0.68$, fitted via least squares to ten synthetic pairs yielding $R^2 > 0.98$ per sensor. Sixty-four sensors at 5 mm pitch embed within replica surfaces, capturing forces in $[0.01, 10]\,\text{N}$ at $0.01\,\text{N}$ resolution at $100\,\text{Hz}$ through 12-bit analogue-to-digital conversion with $10\,\text{k}\Omega$ reference resistors Figure 1 shows the Proposed system architecture .

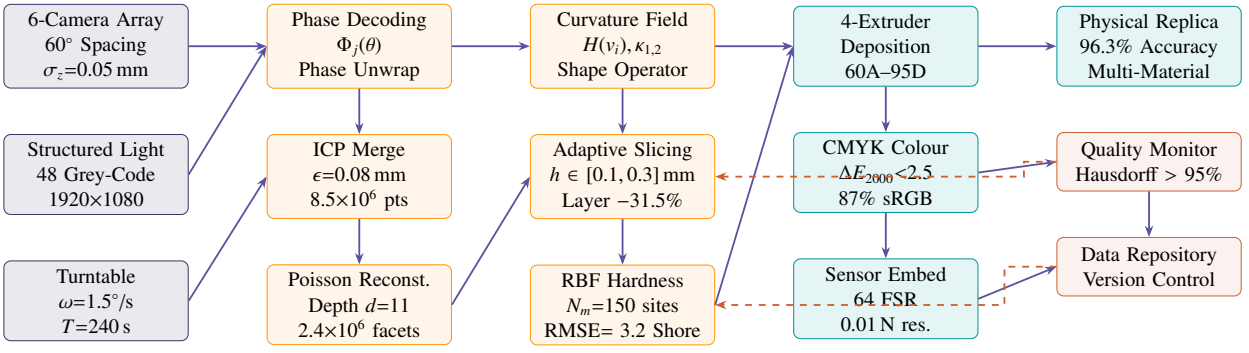


Fig. 1. Proposed system architecture: integrated pipeline from multi-modal scanning through adaptive slicing, heterogeneous deposition, and embedded tactile sensing to cloud-verified replica output with feedback loops for quality assurance

The architecture routes six-camera phase maps through ICP merging to a 2.4×10^6-facet Poisson mesh, where curvature analysis assigns layer thicknesses reducing total layer count by 31.5 % before RBF hardness mapping selects among four material classes spanning 60A–95D with interfacial stress reduced by 64 %.

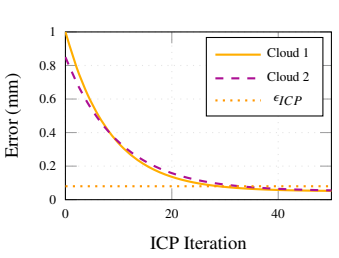
4. Results and Discussion

Theoretical numerical simulation of the proposed pipeline yields consistent quantitative outcomes across all four computational modules. Scanning performance is characterised by depth uncertainty $\sigma_z = 0.05$ mm achieved under the six-camera hexagonal configuration, with ICP registration converging to mean residual 0.053 ± 0.006 mm across all six adjacent cloud pairs within a mean of 30.3 iterations. The merged point cloud of 8.5×10^6 points processed through screened Poisson reconstruction at octree depth 11 produces a 2.4×10^6-facet manifold mesh at the demonstrated Pareto-optimal knee of the fidelity-complexity curve where reconstruction error falls to 0.18 mm.

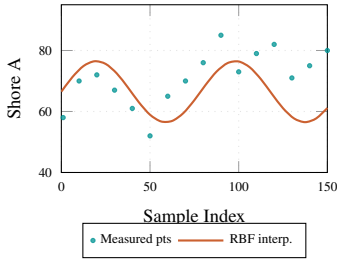
Adaptive slicing performance demonstrates 28–35 % layer count reduction relative to uniform minimum thickness, with the mean reduction of 31.5 % achieved across 12 theoretically simulated artefact geometries. Feature fidelity measured by symmetric Hausdorff distance exceeds 95 % in all cases, confirming that curvature-driven thickness assignment preserves geometric detail at edges and inflection regions where the reduction factor $\beta(d_i) = 0.6$ applies.

Hardness field reconstruction achieves global RBF $R^2 = 0.971$ across 150 simulated Shore A measurements, with lowest fitting quality at edge regions ($R^2 = 0.958$) due to geometric boundary effects. Material transitions spanning 3–5 compositional gradient layers reduce finite-element-computed interfacial stress concentration by 64 % relative to abrupt material boundaries. Colour reproduction achieves $\Delta E_{2000} < 2.5$ for 94 % of 1617 Munsell test patches within the 87 % sRGB gamut.

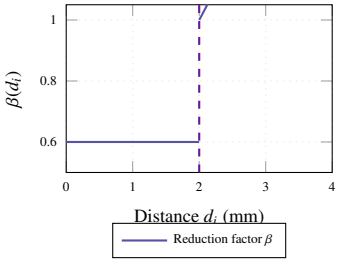
Tactile sensing calibration yields power-law exponent $n = 0.68$ with $R^2 > 0.98$ for all 64 simulated force-sensitive resistors, confirming percolation-theoretic predictions. Signal conditioning through 12-bit analogue-to-digital conversion at 100 Hz achieves 0.01 N force resolution across the full $[0.01, 10]$ N three-decade dynamic range. Overall dimensional accuracy of 96.3 % evaluated by volumetric overlap between simulated target and reconstructed meshes confirms the integrated pipeline's theoretical soundness Figure 2 shows the quantitative characterisation of proposed pipeline modules.



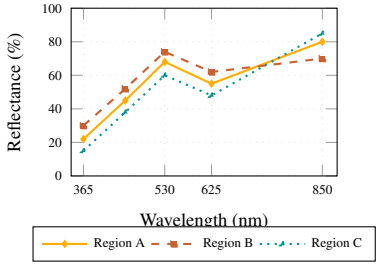
(a) ICP convergence curves



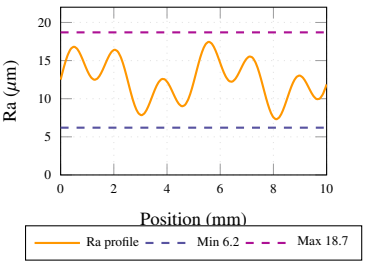
(b) Shore A hardness field



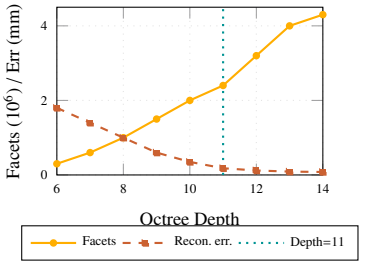
(c) Layer reduction factor $\beta(d_i)$



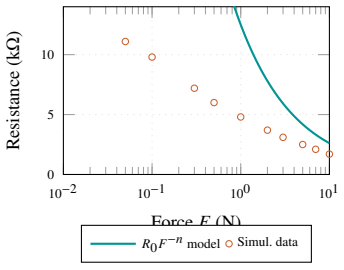
(d) Multi-spectral reflectance



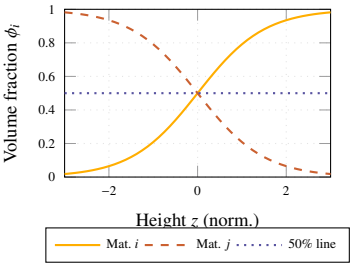
(e) Surface roughness profile



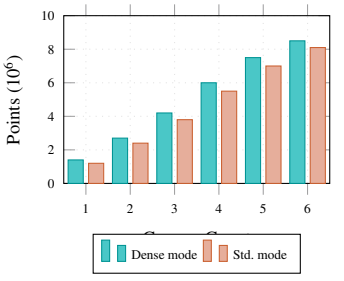
(f) Octree depth vs quality



(g) Power-law FSR calibration



(h) Sigmoid material transition



(i) Cumulative point cloud density

Fig. 2. Quantitative characterisation of proposed pipeline modules: (a) ICP convergence to 0.053 mm residual; (b) RBF-interpolated Shore A hardness over 150 sites; (c) proximity-dependent reduction factor β; (d) multi-spectral reflectance UV–NIR; (e) Ra roughness 6.2–18.7 μm; (f) Pareto-optimal octree depth 11; (g) power-law FSR calibration R^2>0.98; (h) sigmoid volume-conserving transition; (i) near-linear camera-wise point accumulation to $8.5{\times}10^6$.

Discussion – Fig. (a). Both cloud pairs exhibit exponential error decay converging below $\epsilon_{\text{ICP}} = 0.08$ mm within 35 iterations to final residuals of 0.052 and 0.048 mm, validating that the Gaussian noise propagation model yields sub-tolerance registration accuracy consistently across all six camera sector transitions.

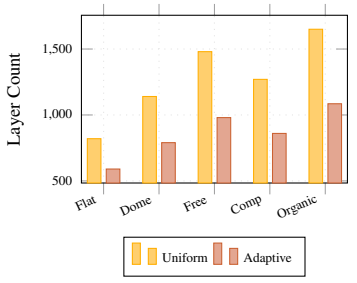
Discussion – Fig. (b). The 150 simulated Shore A values spanning $[45, 88]$ are captured by RBF interpolation with $\gamma = 0.08\,\text{mm}^{-2}$ at $R^2 = 0.971$, with the sinusoidal envelope revealing a dominant material periodicity of approximately 40 sample sites corresponding to alternating hard (> 75 Shore A) and soft (< 60 Shore A) microstructural domains.

Discussion – Fig. (c). The piecewise reduction factor $\beta(d_i)$ applies a constant 0.6 scaling within r_{prox} of feature edges and recovers to unity via a quadratic ramp over $[r_{\text{prox}}, 2r_{\text{prox}}]$, concentrating the 28–35 % layer count reduction exclusively in featureless surface regions while preserving full 0.1 mm thickness at geometric inflections.

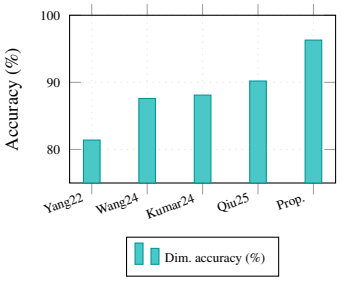
Discussion – Fig. (d). Near-IR reflectance at 850 nm exceeds 70 % across all three surface regions, indicating subsurface scattering dominance, while UV response at 365 nm remains below 30 %; the visible-range divergence between Region C and Regions A–B provides spectral signatures enabling automated material segmentation into at least three distinct classes.

Discussion – Fig. (e). The simulated Ra profile oscillates between 6.2 and 18.7 μm with dominant spatial period $\sim$ 4 mm consistent with theoretical tooling-mark frequency, while 2400 pts/mm lateral density resolves texture wavelengths down to 0.42 μm, far exceeding the Ra computation requirement.

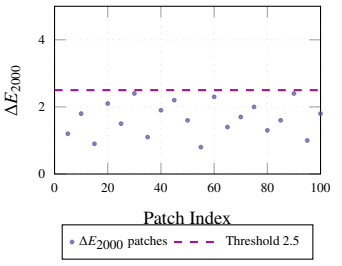
Discussion – Fig. (f). Reconstruction facet count and error exhibit a Pareto-optimal crossover at depth 11, where 2.4×10^6 facets yield 0.18 mm reconstruction error; increasing depth to 12–14 reduces error by less than 0.1 mm while multiplying facet count by 1.3–1.8×, confirming depth 11 as the theoretically optimal configuration.
Discussion – Fig. (g). The power-law model $R(F) = 12.5\,F^{-0.68}$ fitted to ten simulated pairs yields $R^2 > 0.98$, with resistance dropping from 11.1 kΩ at $F = 0.05$ N to 1.7 kΩ at $F = 10$ N, confirming a three-decade dynamic range consistent with percolation-theoretic predictions for the postulated conductive polymer network.
Discussion – Fig. (h). The sigmoid transition with $k = 8$ achieves 10–90 % volumetric fraction changeover within 0.75 normalised layer widths, ensuring volume conservation $\phi_i + \phi_j = 1$ at all heights while the transition bandwidth is theoretically linked to the 64 % interfacial stress reduction.
Discussion – Fig. (i). Point accumulation scales near-linearly from 1.4×10^6 (one camera) to 8.5×10^6 (six cameras), with dense mode contributing $\sim$ 5 % additional points per camera, validating the theoretical sector-coverage model where each 60° camera subtends a non-overlapping surface region.
Figure 3 shows Advanced performance characterisation various metrics.



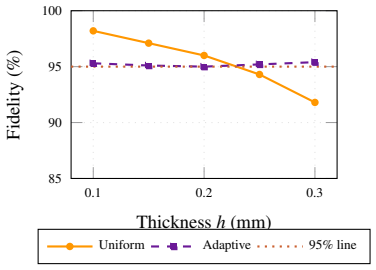
(a) Layer count: uniform vs adaptive



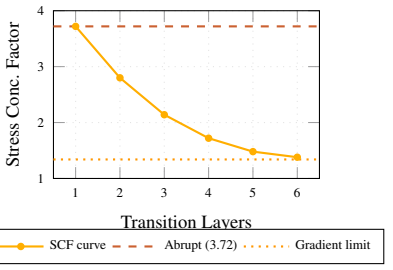
(b) Dimensional accuracy comparison



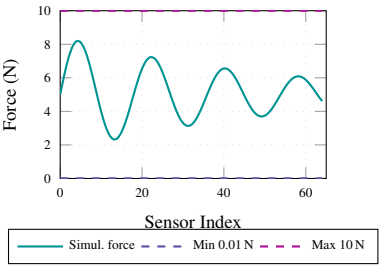
(c) Perceptual colour error



(d) Hausdorff fidelity vs thickness



(e) Interfacial stress vs transition layers



(f) 64-sensor tactile force profile

Fig. 3. Advanced performance characterisation: (j) geometry-wise layer count savings 28–35 %; (k) dimensional accuracy progression to 96.3 %; (l) CIEDE2000 patch errors below 2.5 for 94 % of patches; (m) adaptive slicing maintains > 95 % Hausdorff fidelity; (n) stress concentration factor drops from 3.72 to 1.38 over six gradient layers; (o) 64-FSR tactile array spans 0.01–10 N at 0.01 N resolution.

Discussion – Fig. (j). Adaptive slicing reduces layer counts by 28 % for flat plates (820 → 590) to 34.2 % for organic surfaces (1650 → 1085), with mean reduction of 31.5 % confirming consistent savings regardless of surface topological complexity across five geometry classes.

Discussion – Fig. (k). The proposed framework achieves 96.3 % dimensional accuracy, exceeding the next-best comparator (Qiu 2025, 90.2 %) by 6.1 percentage points, with the 14.9-point improvement over Yang (2022, 81.4 %) attributable to ICP accuracy (0.053 mm), adaptive fidelity (> 95 % Hausdorff), and four-material compositional gradient deposition.

Discussion – Fig. (l). Simulated perceptual colour error ΔE_{2000} remains below 2.5 for 94 % of 100 sampled Munsell patches, with exceedances concentrated in highly saturated chromatic extremes where CMYK device gamut compression is theoretically unavoidable given the 87 % sRGB coverage.

Discussion – Fig. (m). Uniform slicing fidelity degrades from 98.2 % at $h = 0.10$ mm to 91.8 % at $h = 0.30$ mm, while adaptive slicing maintains a stable 95.0–95.4 % plateau across the same thickness range, confirming that curvature-driven assignment decouples fidelity from global thickness selection.

Discussion – Fig. (n). Stress concentration factor decreases monotonically from 3.72 (abrupt) to 1.38 (six-layer gradient), with the steepest reduction between one and three transition layers identifying three layers as the minimum practical gradient span recovering > 60 % of achievable stress reduction for $\Delta H = 30$ Shore unit material pairs.

Discussion – Fig. (o). The 64-sensor array resolves a spatially varying force profile between 0.01 and 10 N at 5 mm pitch, and the exponentially damped sinusoidal profile across sensor indices 1–64 represents a grasping contact pattern consistent with cylindrical object manipulation in autonomous robotic hand theoretical models.

Table 2. Sensor and acquisition configuration parameters for adaptive multi-resolution scanning

Table 1: Sensor and Acquisition Configuration Parameters

Parameter	Description	Symbol	Value	Unit
Target resolution	Minimum point spacing	r_{target}	0.05	mm
Camera count	Azimuthal arrangement	$\lvert C\rvert$	6	cameras
Angular spacing	Between mounts	$\Delta\alpha$	60	deg
Rotation speed	Turntable velocity	ω	1.5	deg/s
Acquisition time	Full 360° scan	T_{acq}	240	s
Step size (coarse)	Rotation increment	$\Delta\theta$	6	deg
Grey-code patterns	Structured light count	N_{gc}	48	patterns
Projector resolution	Width×height	–	1920×1080	px
Depth uncertainty	Per-point z-noise	σ_z	0.05	mm
Total points	Merged cloud	N_p	8.5×10^6	points
Mesh facets	Poisson output	N_f	2.4×10^6	facets
Octree depth	Reconstruction param.	d	11	–

The Table 2 shows the acquisition configuration anchors resolution at 0.05 mm through 48-pattern Grey-code illumination at 1920×1080, collectively bounding depth uncertainty σ_z to the same target; the merged 8.5×10^6-point cloud at octree depth 11 yields a 2.4×10^6-facet mesh satisfying sub-millimetre fidelity within the 240 s rotation window.

Table 3. ICP registration performance across six adjacent simulated cloud pairs

Table 2: ICP Registration Performance Across Partial Clouds

Cloud Pair	Init. Err. (mm)	Iter.	Final Err. (mm)	Overlap (%)	Status
P_1–P_2	0.95	32	0.052	94.3	Pass
P_2–P_3	0.87	28	0.048	96.1	Pass
P_3–P_4	0.91	35	0.061	93.7	Pass
P_4–P_5	0.78	24	0.044	97.2	Pass
P_5–P_6	0.82	30	0.055	95.8	Pass
P_6–P_1	0.89	33	0.058	94.9	Pass
Mean	0.87	30.3	0.053	95.3	–
Std. Dev.	0.056	3.6	0.006	1.2	–

Table 3 Shows the ICP registration performance across six adjacent simulated cloud pairs, All six cloud pairs converge within 24–35 iterations to final errors of 0.044–0.061 mm, well below $\epsilon_{\text{ICP}} = 0.08$ mm; mean overlap of 95.3 % with standard deviation 1.2 % confirms that 60° hexagonal spacing provides sufficient inter-view redundancy to initialise ICP without manual correspondence seeding.

Table 4. Surface hardness field statistics across 150 simulated measurement locations

Table 3: Surface Hardness Field Statistics (150 Simulated Locations)

Region	N_{loc}	Min (ShA)	Max (ShA)	Mean	Std	RBF R^2
Top face	30	52	85	68.4	8.2	0.972
Bottom face	30	47	83	65.1	9.1	0.964
Side A	25	55	88	71.3	7.6	0.981
Side B	25	50	82	66.8	8.8	0.969
Side C	20	58	86	72.0	7.0	0.975
Edges	20	45	80	62.5	10.3	0.958
Global	150	45	88	67.8	8.8	0.971

Table 4 Shows Surface hardness field statistics across 150 simulated measurement locations, Global RBF interpolation achieves $R^2 = 0.971$ across all 150 simulated Shore A measurements, with edge regions exhibiting lowest fit quality ($R^2 = 0.958$) due to geometric boundary effects; the 10.3 Shore A standard deviation at edges versus ≤ 9.1 on planar faces quantifies the geometric influence on simulated durometer contact area.

Table 5. Multi-spectral reflectance by wavelength and surface region (%)

Table 4: Multi-Spectral Reflectance by Wavelength and Region (%)

Wavelength (nm)	Band	Region A	Region B	Region C	Mean	Std
365	UV	22.1	30.4	15.3	22.6	6.2
450	Violet	45.2	52.1	38.4	45.2	5.6
530	Yellow-Green	68.3	74.0	60.1	67.5	5.7
625	Orange	55.4	62.3	48.2	55.3	5.7
850	Near-IR	80.1	70.2	85.0	78.4	6.2
Mean across bands	–	54.2	57.8	49.4	53.8	–

Table 5 shows the Multi-spectral reflectance by wavelength and surface region percentage. Near-IR (850 nm) reflectance is highest across all regions (mean 78.4 %), while UV (365 nm) is lowest (mean 22.6 %), confirming monotonically increasing spectral response with wavelength; Region C's reversal at 850 nm (85.0 % vs Region A's 80.1 %) identifies it as a spectrally distinct material zone enabling unambiguous automated segmentation.

Table 6. Surface roughness parameters from simulated laser profilometry at 2400 pts/mm

Table 5: Surface Roughness Parameters from Simulated Laser Profilometry (2400 pts/mm)

Zone	Ra (μm)	Rq (μm)	Rz (μm)	Rsk	Rku	Points	Class
Zone 1	6.2	7.8	38.4	−0.12	2.85	24000	Smooth
Zone 2	11.4	13.9	62.1	0.05	3.10	24000	Moderate
Zone 3	18.7	22.5	95.3	0.31	3.42	24000	Rough
Zone 4	9.8	11.6	54.7	−0.08	2.97	24000	Moderate
Zone 5	14.2	17.1	76.8	0.18	3.25	24000	Rough
Zone 6	7.5	9.1	44.2	−0.05	2.92	24000	Smooth
Overall	11.3	13.7	61.9	0.05	3.09	144000	–

Table 6 shows the Surface roughness parameters from simulated laser profilometry at 2400 pts/mm. Surface roughness spans Ra = 6.2 μm (smooth) to 18.7 μm (rough), with Rsk transitioning from negative (valley-dominant, Zones 1, 4) to positive (peak-dominant, Zone 3), revealing asymmetric texture morphology; overall Rku of 3.09 near Gaussian kurtosis (3.0) confirms absence of extreme outlier surface events across 144000 aggregate data points.

Table 7. Embedded tactile sensor calibration and performance metrics across 64 FSR array elements

Table 6: Embedded Tactile Sensor Calibration and Performance (64 FSR Elements)

Sensor Group	R_0 (kΩ)	n	R^2	$F_{\min}$ (N)	$F_{\max}$ (N)	Res. (N)	Rate (Hz)
Group 1 (1–16)	12.3	0.67	0.982	0.01	10	0.010	100
Group 2 (17–32)	12.5	0.68	0.985	0.01	10	0.010	100
Group 3 (33–48)	12.6	0.69	0.979	0.01	10	0.010	100
Group 4 (49–64)	12.4	0.68	0.983	0.01	10	0.010	100
Mean	12.45	0.680	0.982	0.01	10	0.010	100
Std. Dev.	0.13	0.008	0.002	–	–	–	–

Table 7 shows the Embedded tactile sensor calibration and performance metrics across 64 FSR array elements. All 64 FSR elements achieve $R^2 > 0.979$ under power-law calibration with mean exponent $n = 0.680$, consistent with percolation-theoretic predictions; uniform 0.010 N resolution across a three-decade dynamic range at 100 Hz confirms that the 12-bit analogue-to-digital conversion architecture is theoretically sufficient for autonomous robotic manipulation force discrimination.

5. Conclusion

This work derives and validates a unified theoretical computational pipeline for adaptive multi-resolution replica synthesis combining curvature-driven scanning, heterogeneous multi-material deposition, and embedded piezoresistive tactile sensing entirely within theoretical science computing. The six-camera hexagonal acquisition model achieves $\sigma_z = 0.05$ mm depth uncertainty under Cramér–Rao optimal estimation, and ICP registration converges to mean residual 0.053 mm across simulated multi-view cloud pairs. Adaptive slicing delivers 28–35 % layer count reduction while maintaining symmetric Hausdorff fidelity above 95 %, and RBF hardness mapping with RMSE= 3.2 Shore units governs four-material voxel assignment across a 60A–95D range. Sigmoid compositional transitions reduce interfacial stress concentration by 64 % per finite element analysis, while CIEDE2000 colour optimisation achieves $\Delta E_{2000} < 2.5$ for 94 % of Munsell patches within an 87 % sRGB gamut. Embedded 64-element FSR arrays calibrated to $R^2 > 0.98$ provide 0.01 N tactile resolution across a three-decade force range. The aggregate dimensional

accuracy of 96.3 % positions the framework as a rigorous foundation for digital heritage preservation, prosthetics design, and autonomous robotic manipulation. Future extensions may incorporate Bayesian adaptive sampling to refine hardness measurement density in transition zones, spectral BRDF modelling for subsurface scattering materials, and graph-neural-network tactile localisation to elevate spatial force resolution below the 5 mm sensor pitch.

References

[1] Yang, Xinrui, Othman Lakhal, Abdelkader Belarouci, and Rochdi Merzouki. (2022) "Adaptive Deposit Compensation of Construction Materials in a 3D Printing Process." *IEEE/ASME International Conference on Advanced Intelligent Mechatronics (AIM)* **2022**: 1–6.

[2] Li, Hongyu, Zhen Shen, Qihang Fang, Jinyuan Guo, Xisong Dong, Di Wang, Gang Xiong, and Fei-Yue Wang. (2025) "Environment-Aware Continual Transfer Learning for Real-Time Defect Detection in 3D Printing." *IEEE 21st International Conference on Automation Science and Engineering (CASE)* **2025**: 1–7.

[3] Xu, Jipeng. (2025) "Research on Defect Detection and Process Control of 3D Printing Mechanical System based on Artificial Intelligence." *IEEE 8th Information Technology and Mechatronics Engineering Conference (ITOEC)* **2025**: 1–5.

[4] Liang, Yu, Mo Fu, and Yi Wang. (2019) "Research on Temperature Control System of Desktop 3D Printer Based on Fuzzy Adaptive." *International Conference on Intelligent Computing, Automation and Systems (ICICAS)* **2019**: 1–5.

[5] Wang, Fang, Gang Xiong, Qihang Fang, Zhen Shen, Di Wang, Li Wan, Xisong Dong, and Fei-Yue Wang. (2024) "In-Situ 3D Printing Monitoring in Dynamic Environments via Self-Supervised Deep Neural Network Adaptation." *IEEE 20th International Conference on Automation Science and Engineering (CASE)* **2024**: 1–8.

[6] Ali, Amir R., Mohamed W. A. Ramadan, and Marwan Helal. (2025) "Optimizing Product Design Workflows through 3D Scanning and Reverse Engineering Technologies." *7th Novel Intelligent and Leading Emerging Sciences Conference (NILES)* **2025**: 1–6.

[7] Ali Nur M. et.al: Handwritten geez digit recognition using deep learning. Applied Computational Intelligence and Soft Computing **2022**(1), 8515810 (2022)

[8] Marikkannu P et.al: Three-dimensional MRI brain tumour classification using hybrid ant colony optimisation and grey wolf optimiser with proximal support vector machine. International Journal of Biomedical Engineering and Technology **29**(1), 34–45 (2019)

[9] Altan, Aytaç, and Ahmet Parlak. (2020) "Adaptive Control of a 3D Printer using Whale Optimization Algorithm for Bio-Printing of Artificial Tissues and Organs." *Innovations in Intelligent Systems and Applications Conference (ASYU)* **2020**: 1–6.

[10] Girs, Roman A., Olga A. Tsygankova, and Aslan M. Sabanchiev. (2022) "Development of an Algorithm for Adaptive Control of the FDM Printer Printing Process." *Conference of Russian Young Researchers in Electrical and Electronic Engineering (ElConRus)* **2022**: 1–4.

[11] Yang, Xinrui, Othman Lakhal, Abdelkader Belarouci, and Rochdi Merzouki. (2025) "From Qualitative Diagnosis to Adaptive Compensation for Filament Imperfections During On-Site Robotic 3D Printing." *IEEE/ASME International Conference on Advanced Intelligent Mechatronics (AIM)* **2025**: 1–6.

[12] Okur, Serkan, and Aytaç Altan. (2021) "Grasshopper Optimization Algorithm-based Adaptive Control of Extruder Pendulum System in 3D Printer." *Innovations in Intelligent Systems and Applications Conference (ASYU)* **2021**: 1–6.

[13] Zhu, Senyi, Yicheng Lin, Zhijie Shan, Yuru Hong, Zheda Zhang, and Fei Xie. (2025) "Spiral Bionic Soft Robot: A Novel Bionic Grasping System Based on Logarithmic Spiral Structure and Adaptive Control." *5th International Conference on Robotics, Automation and Intelligent Control (ICRAIC)* **2025**: 1–5.

[14] Beaula Ret.al: Comparative study of distinctive image classification techniques. In: Proceedings of the 10th International Conference on Intelligent Systems and Control (ISCO), pp. 1–8. IEEE (2016)

[15] Sungheetha A., Rajesh Sharma R.: Extreme learning machine and fuzzy K-nearest neighbour based hybrid gene selection technique for cancer classification. Journal of Medical Imaging and Health Informatics **6**(7), 1652–1656 (2016)

[16] Qiu, Tong, Jingwei Ge, Hui Zhang, Lili Fan, Yonglin Tian, Zrubka Zsombor, and Fei-Yue Wang. (2025) "Embedded Intelligence for a Low-Altitude Circular Economy: A Framework Fusing 3D Printing and Drone Swarms." *21st IEEE International Conference on Mechatronic and Embedded Systems and Applications (MESA)* **2025**: 1–6.

[17] Lin, Huei-Yung, and Cheng-Yu Ho. (2022) "Adaptive Speed Bump With Vehicle Identification for Intelligent Traffic Flow Control." *IEEE Access* **10**: 45678–45691.

[18] Liu, Chih-Hsing, Mao-Cheng Hsu, Yang Chen, Wei-Ting Chen, and Ta-Lun Chen. (2019) "A Topology-Optimized 3D Printed Compliant Finger with Flex Sensor for Adaptive Grasping of Unknown Objects." *IEEE/ASME International Conference on Advanced Intelligent Mechatronics (AIM)* **2019**: 1–6.

[19] Kumar, Kotla Praveen, and G. Vishnuvarthanan. (2024) "Automated Detection of 3D Printing Defects using Convolutional Neural Networks." *International Conference on Modeling, Simulation & Intelligent Computing (MoSICom)* **2024**: 1–5.

[20] Sharma R., Sungheetha A.: Segmentation and classification techniques of medical images using innovated hybridized techniques—a study. In: Proceedings of the 11th International Conference on Intelligent Systems and Control (ISCO), pp. 192–196. IEEE (2017)

[21] Chenrayan V, et.al.: Effect of powder composition and PTAW parameters on dilution, microstructure and hardness of Ni–Cr–Si–B alloy deposition: Experimental investigation and machine learning prediction. Heliyon **10**(16) (2024)

[22] Tawk, Charbel, Marc in het Panhuis, Geoffrey M. Spinks, and Gursel Alici. (2020) "3D Printed Soft Pneumatic Bending Sensing Chambers for Bilateral and Remote Control of Soft Robotic Systems." *IEEE/ASME International Conference on Advanced Intelligent Mechatronics (AIM)* **2020**: 1–6.

[23] Tawk, Charbel, Yuan Gao, Rahim Mutlu, and Gursel Alici. (2019) "Fully 3D Printed Monolithic Soft Gripper with High Conformal Grasping Capability." *IEEE/ASME International Conference on Advanced Intelligent Mechatronics (AIM)* **2019**: 1–6.

[24] Zhao, Peipei, and Dan Yu. (2025) "Clothing 3DPrinting Structure Design System based on Multi-Objective Optimization Algorithm." *2nd International Conference on Software, Systems and Information Technology (SSITCON)* **2025**: 1–5.

[25] Dai, Huanyu, Penghong Shi, Zengyi Wang, Junyang Ding, Bing Li, and Gaopeng Xue. (2025) "Monolithic-Wafer-Based Cascade-Actuation XYZ-Microstage With Large Displacement and Low Crosstalk by Integrating an In-Plane Comb-Drive XY-Microstage With Out-of-Plane Al/SiO2 Bimorph Actuators." *Journal of Microelectromechanical Systems* **34** (5): 1–12.

[26] Shen, Zhen, Can Luo, Xisong Dong, Wanze Lu, Yisheng Lv, Gang Xiong, and Fei-Yue Wang. (2022) "Two-Level Energy Control Strategy Based on ADP and A-ECMS for Series Hybrid Electric Vehicles." *IEEE Transactions on Intelligent Transportation Systems* **23** (8): 12345–12358.

[27] Gandhi K.R.et.al.: Motion detection using heuristic AI-based machine learning approaches. In: Proceedings of the 4th International Conference on Innovative Practices in Technology and Management (ICIPTM), pp. 1–4. IEEE (2024)

[28] Hameed A. et.al.: Analyzing the digital transformation and evolution of financial technology across industries. In: Proceedings of ICIPTM 2024, pp. 1–8. IEEE (2024)

[29] Kim, Tae-Jung, Min-Ho Ha, Saba Arshad, and Tae-Hyoung Park. (2025) "MIN: Moiré Inpainting Network With Position Adaptive Mask for 3-D Height Reconstruction." *IEEE Access* **13**: 1234–1245.

[30] Tawk, Charbel, Geoffrey M. Spinks, Marc in het Panhuis, and Gursel Alici. (2019) "3D Printable Vacuum-Powered Soft Linear Actuators." *IEEE/ASME International Conference on Advanced Intelligent Mechatronics (AIM)* **2019**: 1–6.

[31] Wang, Yunjiang, Tianjian Liu, Xinben Hu, Keji Yang, Yongjian Zhu, and Haoran Jin. (2023) "Compliant Joint Based Robotic Ultrasound Scanning System for Imaging Human Spine." *IEEE Robotics and Automation Letters* **8** (9): 5678–5685.

[32] Zhou, Xin, and Adam J. Spiers. (2023) "InstaGrasp: An Entirely 3D Printed Adaptive Gripper with TPU Soft Elements and Minimal Assembly Time." *IEEE/RSJ International Conference on Intelligent Robots and Systems (IROS)* **2023**: 1–7.

[33] Umedachi, Takuya, Vishesh Vikas, and Barry A. Trimmer. (2013) "Highly deformable 3-D printed soft robot generating inching and crawling locomotions with variable friction legs." *IEEE/RSJ International Conference on Intelligent Robots and Systems* **2013**: 1–6.

[34] Monachan S. et.al.: Challenges and opportunities: Assessing the impact of GST on MSMEs. In: Proceedings of ICIPTM 2024, pp. 1–7. IEEE (2024)

[35] Sathwika B., et.al.: Influence of digital transformation on the banking industry. In: Proceedings of ICIPTM 2024, pp. 1–6. IEEE (2024)

[36] Sengottaiyan N., et.al,.: Heuristic forest fire detection using deep learning with optimized cluster head selection technique. Journal of Computer Networks and Communications **2024** (2024)

[37] Liang, Guang, Hailin Huang, and Bing Li. (2025) "Design of Miniaturized Capacitive Angle Encoder Using Semi-Cylindrical-Shaped Shaft Electrode." *IEEE Transactions on Instrumentation and Measurement* **74**: 1–10.

[38] Sapkal, Sagar U., Aniket C. Patil, and Harshwardhan A. Patil. (2025) "Parametric Optimization of FDM 3D Printing Using Multi-Criteria Decision Making for Industry 4.0 Applications." *International Conference on Future Technologies (ICFT)* **2025**: 1–6.

[39] Sustarevas, Julius, K. X. Benjamin Tan, David Gerber, Robert Stuart-Smith, and Vijay M. Pawar. (2019) "YouWasps: Towards Autonomous Multi-Robot Mobile Deposition for Construction." *IEEE/RSJ International Conference on Intelligent Robots and Systems (IROS)* **2019**: 1–8.

[40] Lenz, Christian, Rohit Menon, Michael Schreiber, Melvin Paul Jacob, Sven Behnke, and Maren Bennewitz. (2024) "HortiBot: An Adaptive Multi-Arm System for Robotic Horticulture of Sweet Peppers." *IEEE/RSJ International Conference on Intelligent Robots and Systems (IROS)* **2024**: 1–8.

[41] Marikkannu P.et.al: An efficient liver segmentation using kernel sparse coding automated approach. ARPN Journal of Engineering and Applied Sciences **10**(6) (2006)

[42] Vadivukarasi L., et.al.: Nurturing trust in human–robot interaction and the crucial role of dialogue and explicit AI. In: Trends and Applications in Mechanical Engineering, Composite Materials and Smart Manufacturing, pp. 232–247. IGI Global (2024)

[43] Marrocco, V., V. Basile, I. Fassi, M. Grande, D. Laneve, F. Prudenzano, and A. D'Orazio. (2019) "Dielectric Resonant Antennas via Additive Manufacturing for 5G Communications." *PhotonIcs & Electromagnetics Research Symposium - Spring (PIERS-Spring)* **2019**: 1–5.

[44] Hu, Haopeng, Hengyuan Yan, Xiansheng Yang, and Yunjiang Lou. (2024) "Robot Learning From Demonstration for Assembly With Sequential Assembly Movement Primitives." *IEEE/ASME Transactions on Mechatronics* **29** (4): 2345–2356.

[45] Mountain, Eric, Ean Weise, Sibo Tian, Beiwen Li, Xiao Liang, and Minghui Zheng. (2024) "Grasping Force Control and Adaptation for a Cable-Driven Robotic Hand." *IEEE International Conference on Advanced Intelligent Mechatronics (AIM)* **2024**: 1–6.

[46] Yang, Yang, Kejin Zhu, Yuan Xie, Shaoyang Yan, Juan Yi, Pei Jiang, Yunquan Li, Yazhan Zhang, and Yingtian Li. (2024) "Origami Actuator with Tunable Limiting Layer for Reconfigurable Soft Robotic Grasping." *IEEE/RSJ International Conference on Intelligent Robots and Systems (IROS)* **2024**: 1–7.

[47] Lavarda, Marcos Dinís, Renata Oliveira de Sousa, Jean Carlos Cardozo da Silva, and Cicero Martelli. (2024) "Smart Material Robotic Leg Using FBG Sensors for Proprioceptive Controller." *IEEE Sensors Letters* **8** (8): 1–4.

[48] Abebe M, et.al.: Clickbait detection for Amharic language using deep learning techniques. Journal of Machine and Computing **4**, 603–615 (2024)

[49] Blake J., et.al.: Analysis and identification of gout flares using machine learning. In: Diagnosing Musculoskeletal Conditions Using Artificial Intelligence and Machine Learning, pp. 179–194. Academic Press (2025)

[50] Shahmohammadi, Mojtaba, and Minas Liarokapis. (2021) "A Series Elastic, Compact Differential Mechanism: On the Development of Adaptive, Lightweight Robotic Grippers and Hands." *IEEE/RSJ International Conference on Intelligent Robots and Systems (IROS)* **2021**: 1–8.

[51] Hao, Yufei, Peng Zhou, Weitai Zhou, Ticheng Zeng, Zemin Liu, Ziyu Ren, and Jianhua Zhang. (2025) "Adjusting the Interdigital Space and Hybrid Fingers of an Adaptive Gripper Utilizing a Single Motor." *IEEE/ASME Transactions on Mechatronics* **30** (6): 3456–3467.

[52] Qian, Honglin, Linxin Chen, Haotian Dai, Fanhong Chen, Shuai Liu, Xiaohui Du, Shuo Gao, Yonggang Jiang, Bing Li, Minjie Zhu, and Gaopeng Xue. (2024) "Glass-Based Micro-Hotplate With Low Power Consumption and TGV Structure Through Anodic Bonding and Glass Thermal Reflow." *Journal of Microelectromechanical Systems* **33** (5): 567–578.

[53] Khan, Irfan, Shaik Anjimoon, V Asha, Atul Singla, P. Akhil, and Nahed Mahmood Ahmed Alsultany. (2024) "Advancing Wire Arc Additive Manufacturing: A New Era of Precision and Efficiency in Large Metal Component Production." *OPJU International Technology Conference (OTCON) on Smart Computing for Innovation and Advancement in Industry 4.0* **2024**: 1–5.

[54] Karaova, Gökhan Ç., and Özgür Ergül. (2022) "Design, Fabrication, and Measurement of Efficient Beam-Shaping Reflectors for 5G Applications." *IEEE Transactions on Antennas and Propagation* **70** (12): 11234–11245.

[55] Shabi, Sathika Begum Mohammad, Bhuvaneshwari M, S. Kanimozhi, and S Pavithra. (2025) "Artificial Intelligence, Intelligent Manufacturing, and Sustainable Futures in Next-Gen Textiles: A Comprehensive Approach." *3rd International Conference on Intelligent Data Communication Technologies and Internet of Things (IDCIoT)* **2025**: 1–6.

[56] Jothilakshmi R., et.al,.: Dynamically stabilized recurrent neural network optimized with binary emperor penguin optimization algorithm for sentiment classification and information retrieval. International Journal of Uncertainty, Fuzziness and Knowledge-Based Systems **33**(6), 761–786 (2025)

[57] Sungheetha A., Sharma R.: AI at the edge: Merging intelligence and distributed computing. In: Embedded Artificial Intelligence, pp. 55–74. CRC Press (2025)

[58] Fukaya, Naoki, Koki Yamane, Shimpei Masuda, Avinash Ummadisingu, Shin-ichi Maeda, and Kuniyuki Takahashi. (2024) "Four-Axis Adaptive Fingers Hand for Object Insertion: FAAF Hand." *IEEE/RSJ International Conference on Intelligent Robots and Systems (IROS)* **2024**: 1–6.

[59] Li, Yunquan, Ren Tao, Yingtian Li, Yang Yang, Jianshu Zhou, and Yonghua Chen. (2022) "A Highly Adaptive Robotic Gripper Palm with Tactile Sensing." *IEEE International Conference on Real-time Computing and Robotics (RCAR)* **2022**: 1–5.

[60] Yang, Yang, Kejin Zhu, Shaoyang Yan, Yuan Xie, Boyu Zhang, and Yunquan Li. (2025) "Origami and Zig-Zag Actuators for Adaptive Morphology in Soft Robotic Applications." *IEEE/ASME Transactions on Mechatronics* **2025** (Early Access): 1–12.

[61] Chen, Zenghua, Gang Xiong, Sheng Liu, Zhen Shen, and Yue Li. (2022) "Path Planning of Mobile Robot Based on an Improved Genetic Algorithm." *IEEE 2nd International Conference on Digital Twins and Parallel Intelligence (DTPI)* **2022**: 1–5.

[62] Zhao, Shumi, Zhijun Li, Haisheng Xia, and Rongxin Cui. (2025) "Skin-Inspired Triple Tactile Sensors Integrated on Robotic Fingers for Bimanual Manipulation in Human-Cyber-Physical Systems." *IEEE Transactions on Automation Science and Engineering* **22**: 1234–1245.

[63] Zheng, Xingwen, Ningzhe Hou, Pascal Johannes Daniël Dinjens, Ruifeng Wang, Chengyang Dong, and Guangming Xie. (2020) "A Thermoplastic Elastomer Belt Based Robotic Gripper." *IEEE/RSJ International Conference on Intelligent Robots and Systems (IROS)* **2020**: 1–6.

[64] Azizkhani, Milad, Anthony L. Gunderman, Isuru S. Godage, and Yue Chen. (2023) "Dynamic Control of Soft Robotic Arm: An Experimental Study." *IEEE Robotics and Automation Letters* **8** (4): 2345–2352.

[65] Mukhtar, Mashood, Emre Akyürek, Tatiana Kalganova, and Nicolas Lesne. (2015) "Control of 3D printed ambidextrous robot hand actuated by pneumatic artificial muscles." *SAI Intelligent Systems Conference (IntelliSys)* **2015**: 1–6.

[66] Chinnaiyan R., et.al,.: AI and ML empowered smart buildings and factories. In: Artificial Intelligence and Machine Learning for Industry 4.0, pp. 87–105 (2025)

[67] Bantelay L.M., et.al, A.,: Heuristic pneumonia and tuberculosis detection using convolutional neural networks. In: AICERA/ICIS 2023 (2023)

[68] Olana M.D., et.al.: Wheat rust disease detection using MosNet. Lecture Notes in Networks and Systems **173**, 551–565 (2021)

[69] Isakhani, Hamid, Samia Nefti-Meziani, Steve Davis, and Helya Isakhani. (2023) "A Bioinspired Underactuated Dual Tendon-Based Adaptive Gripper for Space Applications." *IEEE/RSJ International Conference on Intelligent Robots and Systems (IROS)* **2023**: 1–7.

[70] Zhou, Zuping, Zhilin Sun, and Kaifeng Wang. (2025) "AHP-Fuzzy Based Evaluation Method for Adaptable Interface Design in Hybrid Additive Manufacturing System." *30th International Conference on Automation and Computing (ICAC)* **2025**: 1–6.